Saturation of Alfvén modes in tokamaks

Saturation of Alfvén modes in tokamaks

Roscoe White[1]**, Nikolai Gorelenkov**[1]**, Marina Gorelenkova**[1]**,
Mario Podesta**[1]**, Stephane Ethier**[1] **and Yang Chen**[2]

[1] Plasma Physics Laboratory, Princeton University, PO Box 451, Princeton, NJ 08543, USA
[2] Dept of Physics, University of Colorado, CO, USA

E-mail: rwhite@pppl.gov

CrossMark

Abstract
Growth of Alfvén modes driven unstable by a distribution of high energy particles up to
saturation is investigated with a guiding center code, using numerical eigenfunctions produced
by linear theory and a numerical high energy particle distribution, in order to make detailed
comparison with experiment and with models for saturation amplitudes and the modification
of beam profiles. Two innovations are introduced. First, a very noise free means of obtaining
the mode-particle energy and momentum transfer is introduced, and secondly, a spline
representation of the actual beam particle distribution is used.

Keywords: Alfven modes, tokamaks, saturation, beam particles

(Some figures may appear in colour only in the online journal)

1. Introduction

The effect of Alfvén modes on energetic particles in toka-
maks is important in general, and could be of significance
for ITER [1]. It is necessary to examine mode evolution to
saturation to predict the effect of such modes on high energy
particle transport and to assist in constructing hybrid models
for such transport. Previous work [2–6] using experimentally
determined mode spectra and amplitudes has shown that a
spectrum of Alfvén modes can cause a reduction of the beam
profile to a critical gradient level corresponding to the onset
of stochastic particle loss due to the mode spectrum, with the
mode amplitudes held at a level just above that producing such
loss. This work reports numerical simulation of mode evo-
lution of unstable Alfvén modes to saturation levels and the
resulting effect on beam particle distributions using equilibria
and beam particle distributions generated by TRANSP [7] and
Alfvén eigenfunctions generated by NOVA [8, 9].

Solving the drift kinetic equation in the presence of Alfvén
modes driven unstable by a distribution of high energy parti-
cles and advancing the mode amplitudes and phases in time
is done with the use of a δf formalism, whereby the initial
distribution f_0 is assumed to be a steady state high energy par-
ticle distribution in the absense of the modes, and $f = f_0 + \delta f$
describes the particle distribution in the presence of the
modes. The Hamiltonian is written as $H = H_0 + H_1$ with H_0
giving the unperturbed motion, conserving particle energy E,

toroidal canonical momentum P_ζ, and magnetic moment μ.
By writing the initial particle distribution in terms of these
variables, a simple means of calculating mode-particle energy
and momentum transfer results, giving a very accurate means
of advancing the modes in time. The numerical beam deposi-
tion code NUBEAM in TRANSP produces a list of particles,
giving energy, pitch, and location, which can be used to find the
unperturbed distribution $f_0(E, P_\zeta, \mu)$. This steady state equilib-
rium distribution is thus constructed using beam deposition
analysis, and no assumptions are made regarding how closely
it resembles a Maxwellian [10]. Furthermore, particle classi-
fication in terms of co- and counter- passing, trapped, banana,
confined or lost, etc, is easily given in terms of these variables
[11]. The unstable mode spectrum and eigenfunctions in the
plasma studied are given by NOVA, which has been shown to
agree well with the modes observed in discharges.

High energy particle destabilized Alfvén modes generally
saturate at amplitudes small enough so that the linear eigen-
functions provide a good approximation to the mode structure
for amplitudes up to saturation. We restrict this study to a case
exhibiting saturated mode amplitudes at a well defined mode
frequency, although the formalism can also describe mode
chirping.

In this work we will use as a test case of the method devel-
oped discharge 141711 in NSTX [12] at a time of 470 ms.
In figure 1 are shown the equilibrium, q profile, and radial
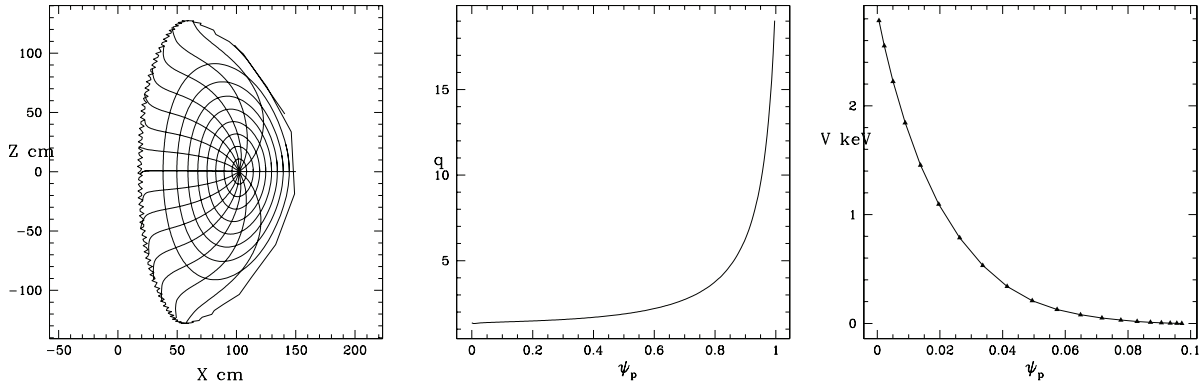potential giving plasma rotation for this case. This discharge

Figure 1. Equilibrium, showing the poloidal cross section with *X* and *Z* in centimeters, the *q* profile, and radial potential for NSTX discharge 141711.

provides an example in which modes grow to a level which modifies the particle distribution without significant change in mode frequency, and with amplitudes which permit the use of linear eigenfunctions. Nonlinear mode–mode coupling is completely negligible, although the particle dynamics involved in driving the modes is fully nonlinear, with modes coupled through their modification of the particle distribution. However, the present work is restricted to the consideration of single modes, mode coupling through the modification of the particle distribution will be addressed in a future publication.

In section 2 we review the guiding center formalism used for the simulation and the low noise method for finding mode-particle energy and momentum transfer. Section 3 shows the important resonances for each of the ten modes present in the discharge. In section 4 the *δf* formalism used is derived, and in section 5 the equations for advancing the mode amplitudes and phases are given. Section 6 gives the means by which energy is transfered from the high energy distribution to the modes, and section 7 is the construction of a splined representation of the beam particle distribution present in the experiment and the results of the simulations. Section 8 shows the method for finding the mode induced modification of the particle distribution with examples for these modes, and section 9 is the conclusion.

2. Guiding center equations

We use units of time given by ω_0^{-1}, where $\omega_0 = eB/(mc)$ is the on-axis gyro frequency, *B* the magnetic field strength, *e* the charge and *m* the particle mass, and units of distance given by the major radius *R*, which was 100 cm, as seen in figure 1. The basic unit of energy becomes $m\omega_0^2 R^2$, which can also be written as $(mv^2/2)(2R^2/\rho^2)$, the gyro radius is $\rho = v/B \ll 1$, and the magnetic moment $\mu = v_\perp^2/(2B)$ is of order ρ^2. Particle motion both along and across the field lines is of order ρ but to leading order the cross field motion is the cyclotron motion, and cross field drift is of order ρ^2 [11].

Equilibrium field quantities are given by $\vec{B} = g\nabla\zeta + I\nabla\theta + \delta\nabla\psi_p$ with ψ_p the poloidal flux, θ a poloidal angle coordinate, ζ a toroidal angle coordinate, and *g*, *I* and δ are equilibrium functions. The Hamiltonian is

$$H_0 = \frac{\rho_\parallel^2 B^2}{2} + \mu B + \Phi \qquad (1)$$

with $\rho_\parallel = v_\parallel/B$, μ the magnetic moment and Φ the electric potential [11]. The toroidal and poloidal canonical momenta are

$$P_\zeta = g(\psi_p)\rho_\parallel - \psi_p, \quad P_\theta = \rho_\parallel + \psi, \qquad (2)$$

with ψ the toroidal flux, and $d\psi/d\psi_p = q(\psi_p)$, the field line helicity.

Guiding center equations advance the variables ψ_p, θ, ζ, and $\rho_\parallel$, leaving μ a constant of the motion. The energy *E* must be recalculated after each time step and the accuracy of energy conservation in the absense of time dependent modes is used to control the time step.

Introduce a magnetic field perturbation of the form $\delta\vec{B} = \nabla \times \alpha\vec{B}$. This form also requires introducing an electric potential Φ, discussed in section 5. We then find [13][3] for the exchange of energy and momentum between the particle distribution and the modes

$$\frac{dH}{dt} = \partial_t H = -\rho_\parallel B^2 \partial_t\alpha + \partial_t\Phi, \quad \frac{dP_\zeta}{dt} = -\partial_\zeta H = \rho_\parallel B^2 \partial_\zeta\alpha - \partial_\zeta\Phi. \qquad (3)$$

Because of the small value of α, the terms in equations (3) are typically four orders of magnitude smaller than those for stepping the four particle variables ψ_p, θ, ζ, and $\rho_\parallel$, and thus these equations are much more accurate than the numerically found energy and momentum changes calculated from the stepped variables, which depend on the cancellation of large terms. In particular, a time independent perturbation will result in a lack of particle energy conservation due to numerical error, whereas the energy transfer by equation (3) is exactly zero. Similarly, an axisymmetric perturbation will erroneously result in modification of P_ζ but equation (3) will give exactly zero. With a general perturbation the values of particle energy and canonical momentum obtained by stepping ψ_p, θ, ζ, and $\rho_\parallel$ will always contain a significant amount of noise as compared to the values given by equations (3). Of course to evaluate equations (3) the particles must be advanced in the four dimensional space of ψ_p, θ, ζ, $\rho_\parallel$ and the energy transfer is

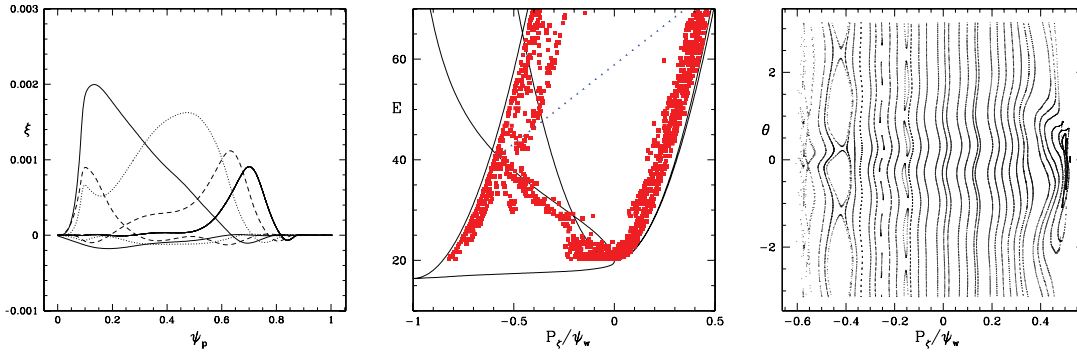[3] See also equation (3.102) in [3].

Figure 2. Harmonics, resonance domains, and a sample Poincaré plot, mode 1, $n = 2$, 103 kHz, $\mu B = 20$ keV.

evaluated at the particle location in this space, the improved accuracy is only in the value of the energy transferred to the modes, not in the particle orbits. But to study mode growth and saturation, it is precisely the energy and momentum transfered to the modes which is of interest. Using changes in particle energy and momentum to find the transfer to the modes depends on subtracting terms of order one to obtain terms of order α, typically four orders of magnitude smaller.

Kinetic Poincaré plots, made following high energy particle orbits in the presence of a perturbation with a single toroidal mode number and frequency, and recording points whenever $n\zeta - \omega t = 2\pi k$ with k integer, indicate mode-particle resonances and the island structure of these resonances. Location of mode-particle resonances is also a very delicate process requiring high accuracy [14–16]. In the presence of a single mode, with α and the Hamiltonian functions of $n\zeta - \omega t$ we have

$$\omega \dot{P}_\zeta = n\dot{H}. \tag{4}$$

For a single mode this condition restricts the motion of particles in the P_ζ, E plane to a line $nE - \omega P_\zeta =$ constant, (E, the energy, is the value of the Hamiltonian) due to the action of a mode, defining the possible diffusion in this plane.

Including collisions μ is not constant, and using $\mu = v_\perp^2/(2B)$ and $\lambda = v_\parallel/v$ we find

$$\mathrm{d}\mu = \frac{2E}{B}\lambda \mathrm{d}\lambda \tag{5}$$

and a simple energy conserving pitch angle scattering operator can be used for the changes in λ. In addition, a slowing down operator giving the slowing of high energy particles due to collisions with electrons can easily be included.

3. Resonance determination

A general method for numerically determining the existence of or the destruction of good KAM [17] surfaces can be obtained using the method of phase vector rotation [14–16]. Consider following two orbits located nearby one another. Examine a Poincaré section in P_ζ, θ and define the angle χ to give the orientation of the vector joining them in this plane. If good KAM surfaces exist χ can change by at most an angle of π, due to their relative velocity in the angular coordinate.

However two orbits within an island rotate around one another with χ increasing with the rotation about the island O-point, also referred to as the bounce frequency of a particle trapped in the wave, which increases with the size of the island. The rate of change of χ is a function of distance from the island O-point, dropping to zero at the separatrix.

In figures 2–11 are shown the harmonic content, the location of resonances in the P_ζ, E plane determined by this method, as well as a Poincaré plot shown along the line $E - P_\zeta n/\omega = E_0$ in this plane for the ten modes of the discharge. The constant E_0 is simply the particle energy in the frame rotating with the mode. The points in the P_ζ, E plane clearly indicate the major resonances shown in the Poincaré plots. For this evaluation the magnetic moment was constant, with $\mu B = 20$ keV, where the distribution is strongly peaked. Here and in the following, B in these expressions refers to the value at the magnetic axis, so μB is a constant, simply converting the value of the magnetic moment to units of energy. This method can be used to examine the resonance locations for any value of μB, and sometimes this can be instructive. The method of phase vector rotation can be used with many values of μ present, but for comparison with a Poincaré plot a single value of μ must be selected, and the Poincaré plot shows the resonances only along the line $E - P_\zeta n/\omega = E_0$.

The modes differ significantly regarding the location of the major resonances. In figure 2 we see that there is a major resonance in mode 1, seen both in the P_ζ, E plane and in the Poincaré plot near the left bounding surface, which corresponds to the plasma edge. The right hand edge corresponds to the magnetic axis. The triangle shaped region at the bottom of these plots is the domain of trapped particles. Mode 2, shown in figure 3, also has a significant resonance near the plasma edge, but a stronger one more near the plasma center. These plots give insight as to what kinds of beam particle redistribution each mode is capable. Modes 2,4,6,7,9,10 have strong resonance in the center of the domain of canonical momentum, extending over a large range of energy. Modes 1,5,8 and 9 have strong resonances very near the magnetic axis.

The domains of broken KAM surfaces depend on the existence of a resonance, but this is not sufficient. It is also necessary that a relevant harmonic be reasonably large at the radius at which the resonance occurs. Particle orbits, because of drift motion, do not stay on a particular flux surface. But harmonic
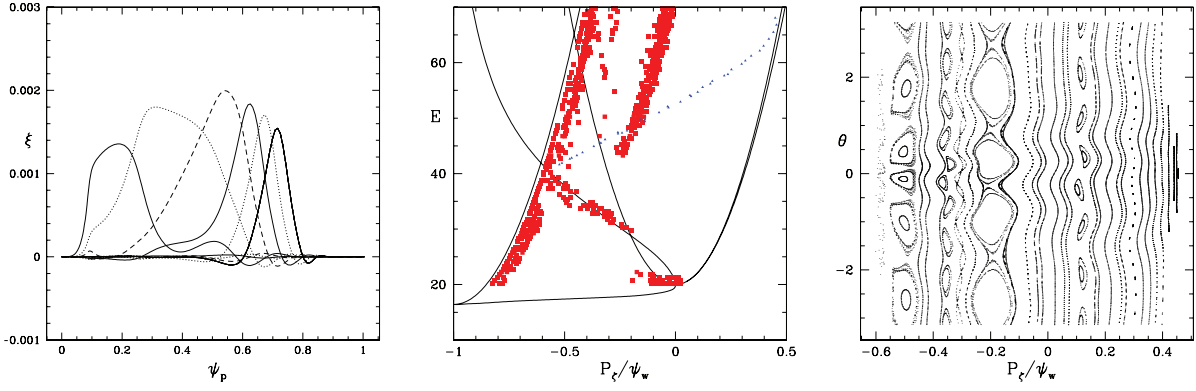
Figure 3. Harmonics, resonance domains, and a sample Poincaré plot, mode 2, $n = 3$, 104 kHz, $\mu B = 20$ keV.

amplitudes are functions of the flux surface, and can be localized, thus a particle can move in and out of the region where the amplitude is large in a single orbital transit. Thus analytic estimates of resonance are not reliable, and methods which exist [18, 19] depend on integration over actual particle orbits.

4. Delta *f* formalism

Now consider mode evolution using a δf procedure. We assume the initial particle distribution is in steady state through the processes of slowing down, collisions, and a continuous source, which could be either beam injection or alpha particle production. Write the particle distribution as $f = f_0 + \delta f$ where the distribution in the absence of the modes f_0 is a function of E, P_ζ, μ, and is independent of time, and the modification of the distribution δf is due to the modes. Following particle orbits

$$\frac{\mathrm{d}}{\mathrm{d}t} f = 0. \tag{6}$$

Then to order α, ν, using the fact that $\dot{E}$ and $\dot{P}_\zeta$ are order alpha and $\dot{\mu}$ is of order ν

$$\frac{\mathrm{d}}{\mathrm{d}t}\delta f = -[\partial_E f_0 \dot{E} + \partial_{P_\zeta} f_0 \dot{P}_\zeta + \partial_\mu f_0 \dot{\mu}] = -R, \tag{7}$$

where $\dot{E}$ and $\dot{P}_\zeta$ refer to a single eigenmode, N, with definite values of n and ω, but which may consist of many poloidal harmonics. The full change in the distribution is given by the sum over all eigenmodes present. However, we assume that the distribution f_0 is in steady state through the combination of collisions and beam injection, and thus for the time evolution of δf we do not include the term $\partial_\mu f_0 \dot{\mu}$. The modification of the particle distribution of interest is that due to the modes only.

Now define a marker distribution function in extended phase space [20], $F(\psi_p, \theta, \zeta, \rho_\parallel, w, t)$ with w the particle weight, and

$$\frac{\mathrm{d}}{\mathrm{d}t} F + \partial_w(\dot{w} F) = 0. \tag{8}$$

In the simulation F has the Klimontovich representation

$F(\psi_p, \theta, \zeta, \rho_\parallel, t)$
$$= \sum_j \delta(\psi_p - \psi_{p,j}(t))\delta(\theta - \theta_j(t))\delta(\zeta - \zeta_j(t))\delta(\rho_\parallel - \rho_{\parallel,j})\delta(w - w_j(t)), \tag{9}$$

with j the particle index and $g(\psi_p, \theta, \zeta, \rho_\parallel, t) = \int \mathrm{d}w F$ is the numerically loaded and evolved distribution function and δf is represented by

$\delta f(\psi_p, \theta, \zeta, \rho_\parallel, t)$
$$= \sum_j w\delta(\psi_p - \psi_{p,j}(t))\delta(\theta - \theta_j(t))\delta(\zeta - \zeta_j(t))\delta(\rho_\parallel - \rho_{\parallel,j}(t)). \tag{10}$$

Integrating equation (8) over w we confirm that $\frac{\mathrm{d}}{\mathrm{d}t} g = 0$. Multiply equation (8) by w and integrate by parts. We then find

$$\int \mathrm{d}w w \dot{F} = \int \mathrm{d}w \dot{w} F. \tag{11}$$

Thus

$$\frac{\mathrm{d}}{\mathrm{d}t}\delta f = \int \mathrm{d}w \dot{w} F, \quad \int \mathrm{d}w \dot{w} F = -R. \tag{12}$$

Try a solution of the form $\dot{w} = (a - bw)(-R)$, giving $ag(E, P_\zeta, \mu, t) - b\delta f(E, P_\zeta, \mu, t) = 1$. Write $g = g_0 + \delta f$, giving $a = b = 1/g_0$, so

$$\frac{\mathrm{d}w}{\mathrm{d}t} = \frac{w - 1}{g(\psi_p, \theta, \zeta, \rho_\parallel, 0)} R. \tag{13}$$

This formulation is extremely useful, as it does not require consideration of the time evolution of the marker distribution, and using the form of R the evolution of w is given by the expressions $(\dot{E}/g_0)\partial_E f_0$ and $(\dot{P}_\zeta/g_0)\partial_{P_\zeta} f_0$. Normally simulations assume that the initial perturbation of the distribution δf is zero, so initially $w(0) = 0$.

5. Mode stepping

The equilibrium magnetic field is given by

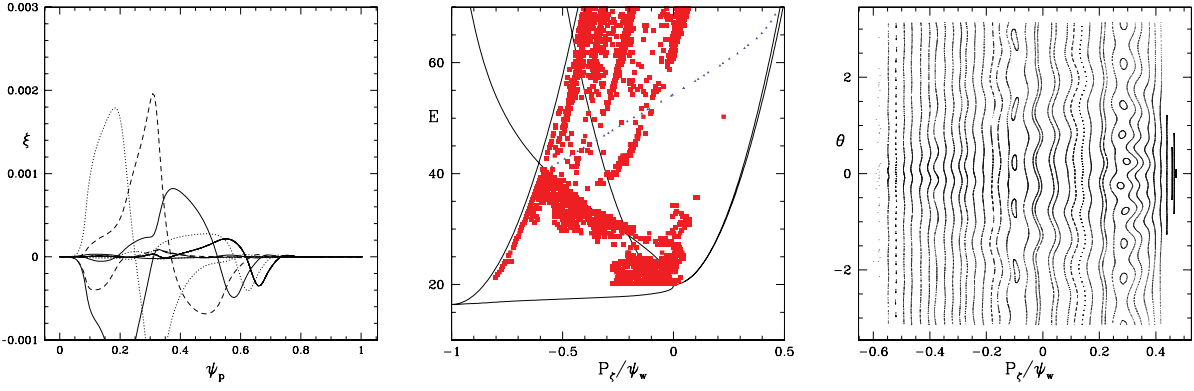$$\vec{B} = g\nabla\zeta + I\nabla\theta + \delta\nabla\psi_p, \tag{14}$$

Figure 4. Harmonics, resonance domains, and a sample Poincaré plot, mode 3, $n = 4$, 155 kHz, $\mu B = 20$ keV.

and in an axisymmetric equilibrium using Boozer coordinates g and I are functions of ψ_p only. The perturbation has the form

$$\alpha = \sum_{m,n} A_n \alpha_{m,n}(\psi) \sin(\Omega_{mn}), \qquad \Phi = \sum_{m,n} A_n \Phi_{m,n}(\psi) \sin(\Omega_{mn}),$$
(15)

where n refers to a single mode with definite toroidal mode number and frequency, but many poloidal harmonics m and $\Omega_{mn} = n\zeta - m\theta - \omega_n t - \phi_n$, with ϕ_n the mode phase, and for ideal modes the electric potential Φ is chosen to cancel the parallel electric field induced by $\mathrm{d}\vec{B}/\mathrm{d}t$, requiring

$$\sum_{m,n} \omega B \alpha_{m,n} \cos(\Omega_{mn}) - \vec{B} \cdot \nabla \Phi / B = 0.$$

and in Boozer coordinates

$$(gq + I)\omega \alpha_{mn} = (nq - m)\Phi_{mn}.$$

The perturbation α is related to the ideal displacement $\vec{\xi}$,

$$\alpha_{mn} = \frac{(m/q - n)}{(mg + nI)} \xi_{mn}^\psi.$$

The numerically produced eigenfunctions are normalized with the largest harmonic $\xi_{mn}^\psi(\psi_\mathrm{p})$ having maximum amplitude 1. Thus the amplitude A_n is the magnitude of the ideal displacement caused by this harmonic, normalized to the major radius R.

Stepping equations for modes were previously derived [20], but in that derivation the $\vec{\xi}_{mn}$ formed an orthonormal basis, not a possible choice for the case of a single mode comprising several poloidal harmonics with fixed relative amplitudes. Stepping in time of the displacement

$$\vec{\xi} = \sum_{mn} A_n \vec{\xi}_{mn}(\psi_\mathrm{p}) \sin(\Omega_{mn})$$
(16)

is given by

$$\sum_{mn} 2\omega_n \vec{\xi}_{mn}(\psi_\mathrm{p})[\dot{A}_n \cos(\Omega_{mn}) + A_n \dot{\phi}_n \sin(\Omega_{mn})] = -\nu_\mathrm{A}^2 \vec{S}$$
(17)

where the frequency ν_A is the local Alfvén frequency and the source $\vec{S}$ is related to mode-particle energy transfer through

$$\vec{v} \cdot \vec{E}_n = A_n \omega_n \sum_m \vec{S} \cdot \vec{\xi}_{mn}(\psi_\mathrm{p}) \cos(\Omega_{mn}),$$

$$\vec{v} \cdot \partial_t \vec{E}_n = A_n \omega_n^2 \sum_m \vec{S} \cdot \vec{\xi}_{mn}(\psi_\mathrm{p}) \sin(\Omega_{mn})$$
(18)

and $\vec{E}_n$ is the electric field corresponding to the displacement $\vec{\xi}_n = \sum_m \vec{\xi}_{mn} \sin(\Omega_{mn})$,

$$\vec{E}_n = A_n \omega_n (\vec{\xi}_n \times \vec{B}) \cos(\Omega_{mn}).$$
(19)

Multiply equation (17) by $\sum_m \vec{\xi}_{mn}(\psi_\mathrm{p}) \cos(\Omega_{mn})$ and $\sum_m \vec{\xi}_{mn}(\psi_\mathrm{p}) \sin(\Omega_{mn})$ and integrate over $\psi_\mathrm{p}, \theta, \zeta$, giving

$$D_n \omega_n \dot{A}_n = -\nu_\mathrm{A}^2 \sum_m \int \vec{S} \cdot \vec{\xi}_{mn}(\psi_\mathrm{p}) \cos(\Omega_{mn}) \mathrm{d}\psi_\mathrm{p} \mathrm{d}\theta \mathrm{d}\zeta,$$
(20)

$$D_n \omega_n A_n \dot{\phi}_n = -\nu_\mathrm{A}^2 \sum_m \int \vec{S} \cdot \vec{\xi}_{mn}(\psi_\mathrm{p}) \sin(\Omega_{mn}) \mathrm{d}\psi_\mathrm{p} \mathrm{d}\theta \mathrm{d}\zeta$$
(21)

with $D_n = 4\pi^2 \sum_m \int \xi_{mn}^2(\psi_\mathrm{p}) \mathrm{d}\psi_\mathrm{p}$. Now use equations (18) and the fact that $\vec{v} \cdot \vec{E}_n$ is the energy transfer between mode and particle, given by $\mathrm{d}H/\mathrm{d}t = -\rho_\parallel B^2 \partial_t \alpha + \partial_t \Phi$, and use the Klimontovich representation for the particle distribution to do the integrals, giving

$$\frac{\mathrm{d}A_n}{\mathrm{d}t} = \frac{-\nu_\mathrm{A}^2}{D_n \omega_n A_n} \sum_{j,m} w_n [\rho_\parallel B^2 \alpha_{mn}(\psi_\mathrm{p}) - \Phi_{mn}(\psi_\mathrm{p})] \cos(\Omega_{mn}) - \gamma_\mathrm{d} A_n,$$
(22)

$$\frac{\mathrm{d}\phi_n}{\mathrm{d}t} = \frac{-\nu_\mathrm{A}^2}{D_n \omega_n A_n^2} \sum_{j,m} w_n [\rho_\parallel B^2 \alpha_{mn}(\psi_\mathrm{p}) - \Phi_{mn}(\psi_\mathrm{p})] \sin(\Omega_{mn}),$$
(23)

with j the particle index and $\psi_\mathrm{p}, \theta, \zeta$ is the position of particle j. The linear damping rate γ_d is due to the continuum, electron and thermal ion Landau damping, and radiation, and all terms in the sums are evaluated at the coordinates of particle j, and w_n the weight of particle j for mode n. Note that there are extra factors of A_n in the denominator compared to [20] because also the weight w_n is proportional to A_n. Note also that particle collisions and slowing down refer to collisions with a background particle species, not to particle-mode transfer. Thus for use in the mode stepping equations the weights are not stepped using the drive resulting from $\partial_\mu f \dot{\mu}$. Collisions and
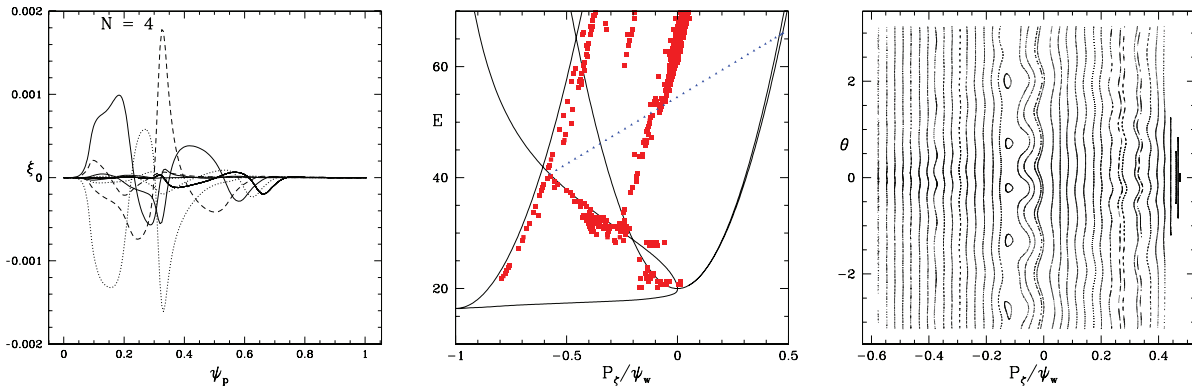
Figure 5. Harmonics, resonance domains, and a sample Poincaré plot, mode 4, $n = 4$, $158\,\mathrm{kHz}$, $\mu B = 20\,\mathrm{keV}$.
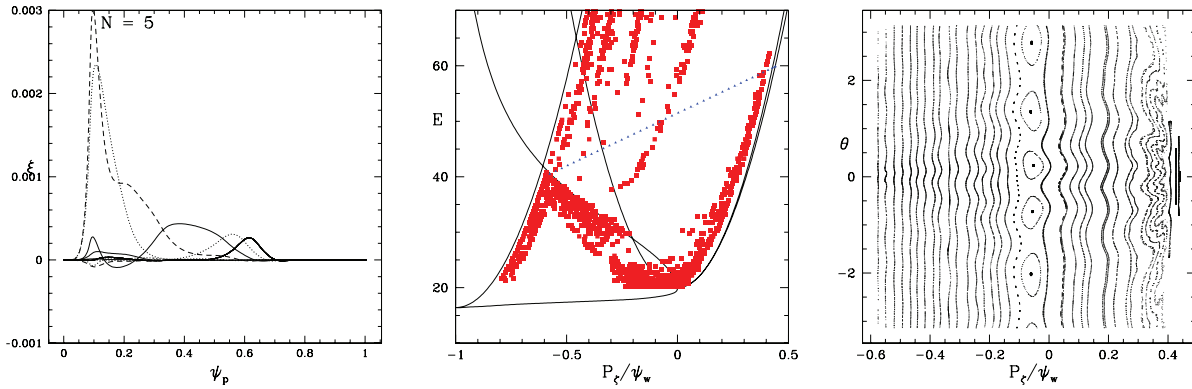

Figure 6. Harmonics, resonance domains, and a sample Poincaré plot, mode 5, $n = 4$, $125\,\mathrm{kHz}$, $\mu B = 20\,\mathrm{keV}$.
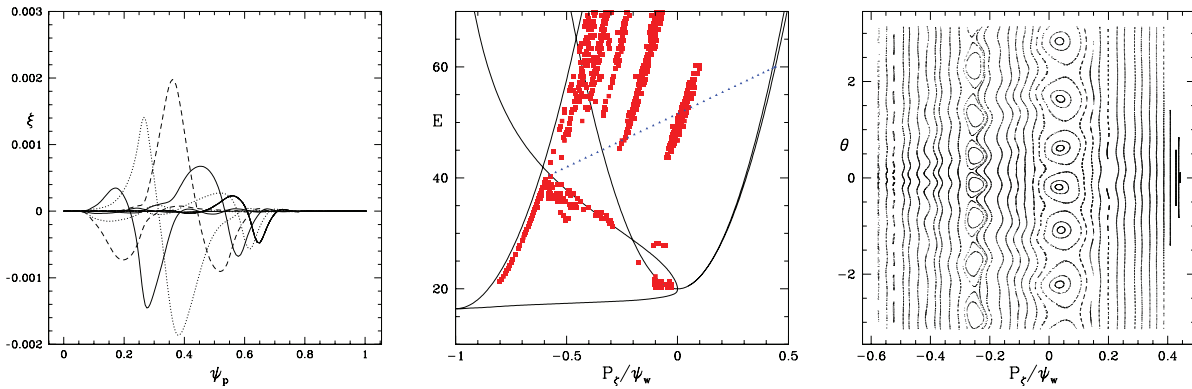
Figure 7. Harmonics, resonance domains, and a sample Poincaré plot, mode 6, $n = 5$, $157\,\mathrm{kHz}$, $\mu B = 20\,\mathrm{keV}$.

slowing down only affect the mode evolution by moving particles in and out of the resonances.

The time evolution of the phase ϕ_n produced by the particle distribution is equivalent to a modification of the mode frequency through $\omega + \dot{\phi}_n$, and can describe mode chirping.

6. Mode-particle energy exchange

In figure 12 is shown the result of a simulation showing the evolution of the mode growth rate with a given initial distribution, no particle source, collisions or slowing down.

The mode amplitude was fixed at a value giving a large resonance. It is seen that the growth rate drops to zero in the bounce time of trapped particles in the mode, at which point the energy and momentum densities in the island have been completly flattened, leaving nothing to further drive the mode. The first Poincaré plot shows the resonant island structure, using 1000 toroidal transits to make the structure clear. The transit time is simply the time for a toroidal transit of a particle with characteristic energy at the magnetic axis with pitch equal to one. The second Poincaré plot shows two particle trajectories trapped in the resonance for the time it takes for the growth rate to drop to zero, forty transits,
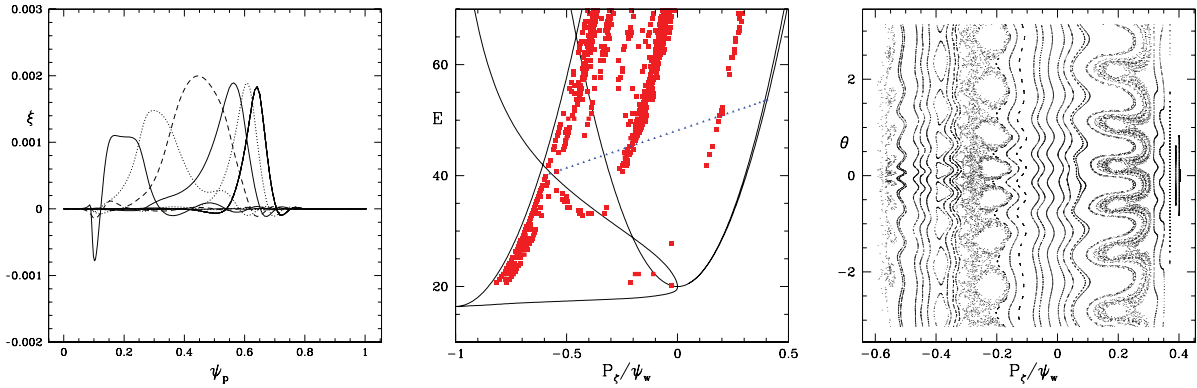
Figure 8. Harmonics, resonance domains, and a sample Poincaré plot, mode 7, $n = 5$, 111 kHz, $\mu B = 20$ keV.
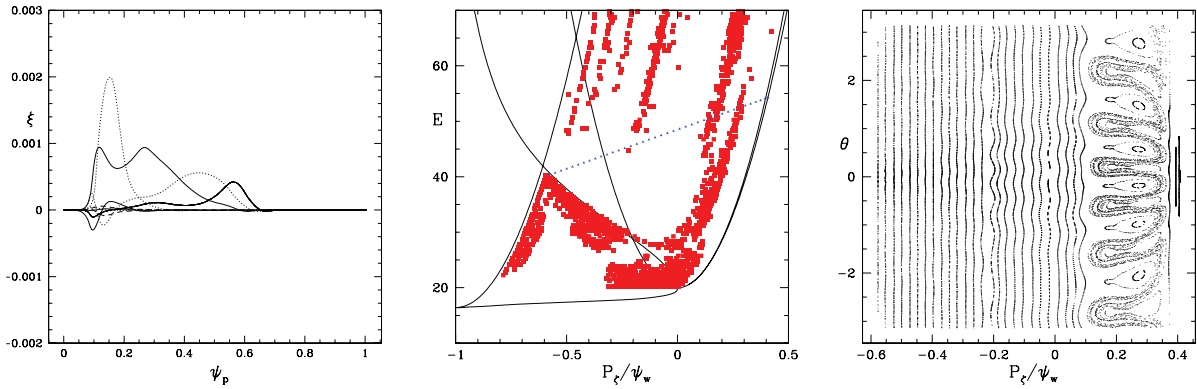

Figure 9. Harmonics, resonance domains, and a sample Poincaré plot, mode 8, $n = 5$, 116 kHz, $\mu B = 20$ keV.
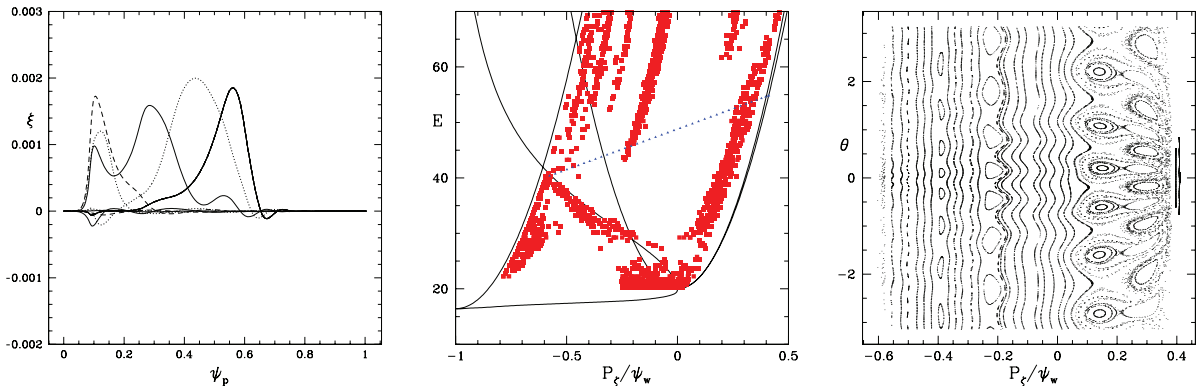

Figure 10. Harmonics, resonance domains, and a sample Poincaré plot, mode 9, $n = 5$, 120 kHz, $\mu B = 20$ keV.

showing that this is simply the mean bounce time in the resonance. The bounce time is shorter for larger islands, and thus larger islands flatten the distribution more quickly. Because the bounce time sepends on distance from the resonance elliptic point, rotation about this point produces fine scale mixing, leading irreversibly to a state of higher entropy. The time scale for mode saturation is much shorter than the time scale for equilibrium changes. But a steady state high energy distribution, because of slowing down and collisions, must be continually maintained by a source. In the case of a beam profile the source is beam injection, in the case of alpha particles it is the fusion source.

The δf formalism produces the same result through the particle weights. In figure 13 is shown the kinetic Poincaré plot of a particle trapped in resonance, for fixed mode amplitude and no particle collisions or slowing down. Also shown is the particle weight as a function of time. The weight grows rapidly until the particle has completed a bounce time, after which it no longer changes, the total mode drive having been extracted. Additional drive to the mode can come only from new particles entering the resonance, through scattering, energy loss through drag, or through mode growth, increasing the size of the island.

Note that these simulations are very different from simulations of electrostatic or electromagnetic turbulence, where
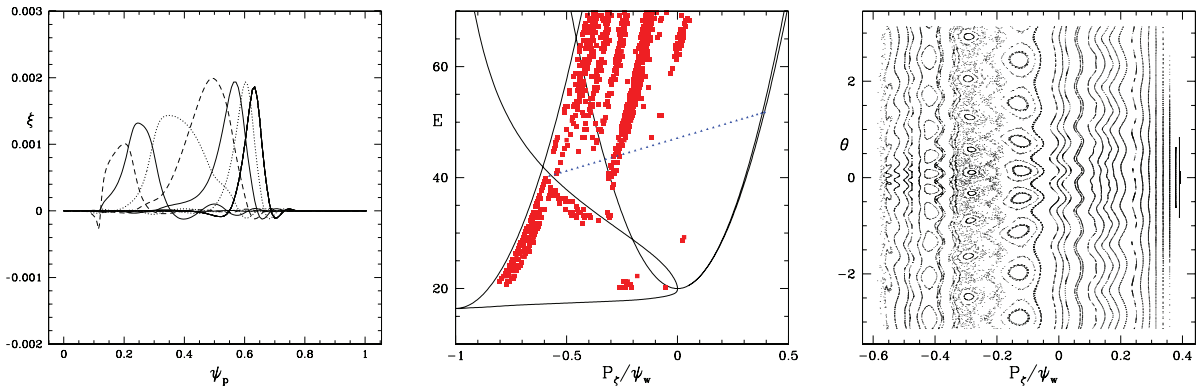
Figure 11. Harmonics, resonance domains, and a sample Poincaré plot, mode 10, $n = 6$, $116\,\text{kHz}$, $\mu B = 20\,\text{keV}$.
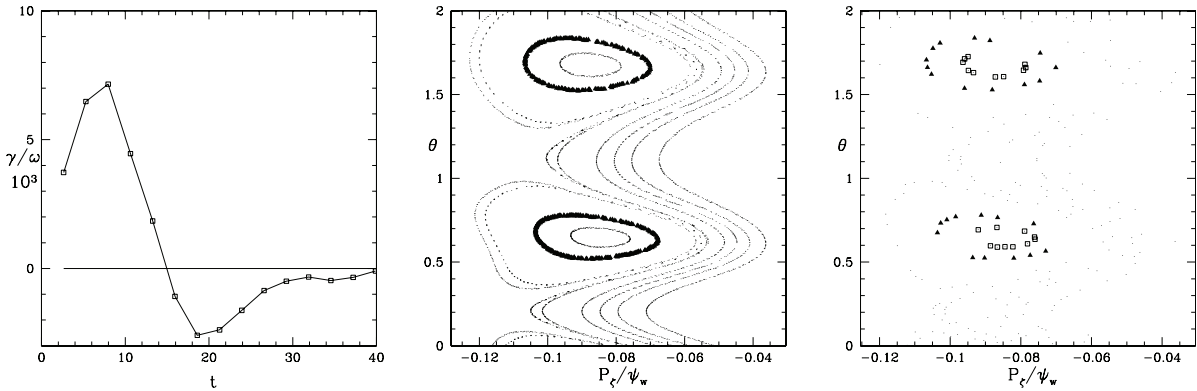

Figure 12. γ/ω versus time, Poincaré plots with 1000 transits and 40 transits. In one bounce time the distribution in an island is flattened, and if the amplitude is fixed and there are no collisions or slowing down of particles, causing them to enter or leave resonance, the mode drive stops.
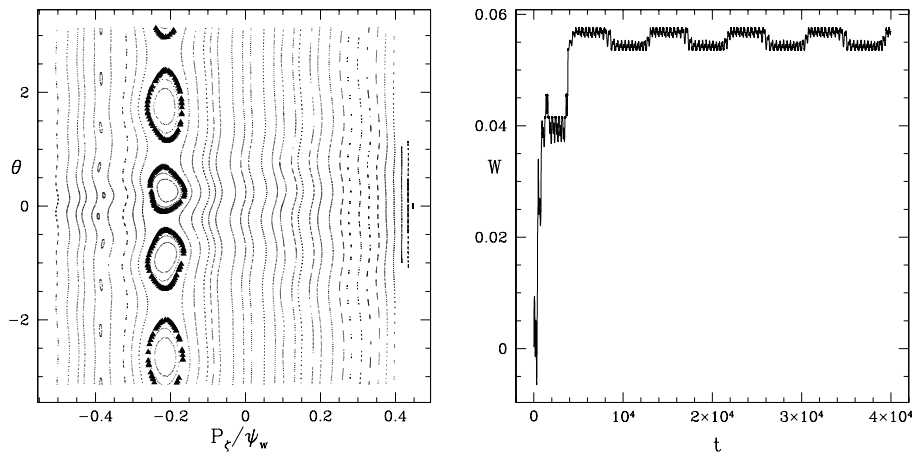

Figure 13. Evolution of particle weight in resonance.

resonances are continually appearing and disappearing as the fields change. In the present situation the resonances are very stable results of the high energy particle distribution and are essentially constant over the whole simulation except for becoming larger as the amplitudes grow, unless nearby resonances overlap, producing larger stochastic domains. In this case it is not simple resonance bounce time that determines the time scale for distribution flattening, but the time scale for stochastic transport.

7. Numerical method for the general case

The variables determining mode growth and saturation are the drive, given by partial derivatives of f and the slowing down and collision frequencies and the damping. Growth is determined by an imbalance between the rate at which free energy is introduced into the island and the mixing rate, and saturation occurs when the island grows to a point where these rates are balanced [21]. Saturation occurs because the
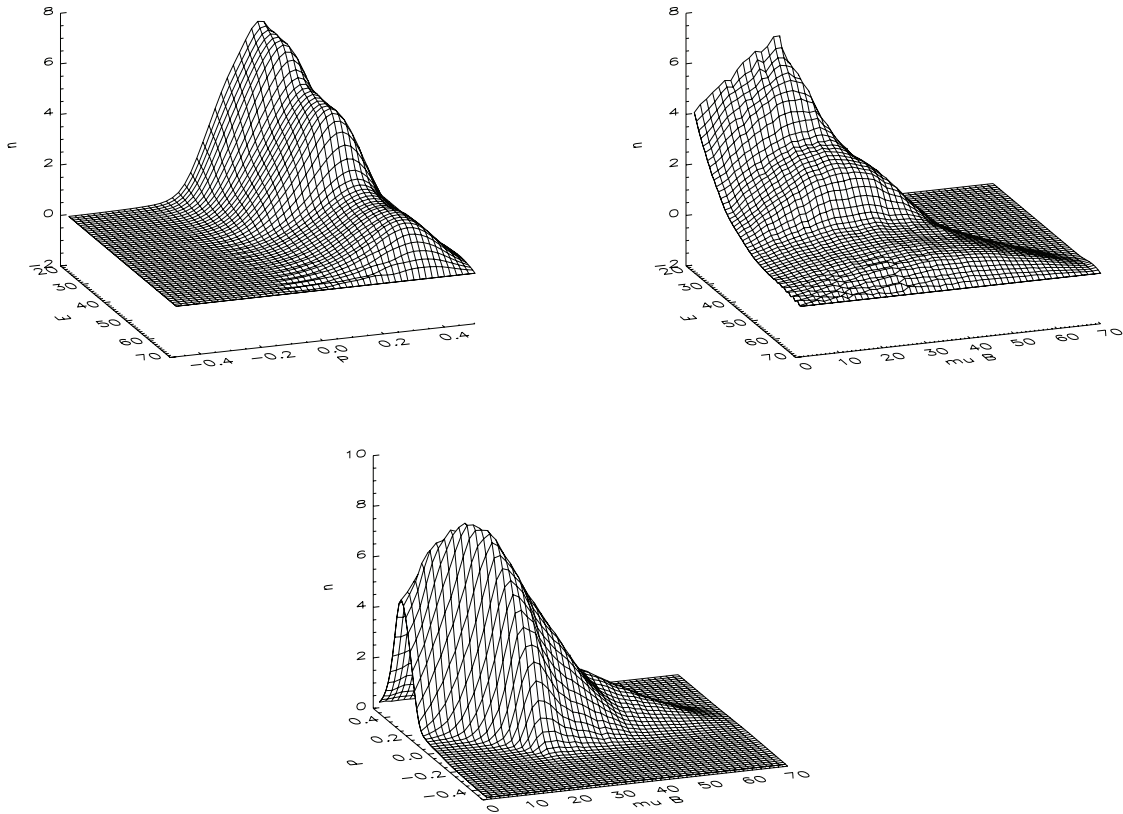
Figure 14. Example NSTX beam distribution for shot 141711. The energy E ranges from 20 to 70 Kev, and the value of μB from 0 to 70 Kev. The canonical momentum P_ζ/ψ_w ranges from $-.5$ to $.5$. In each plot the third variable is summed over.
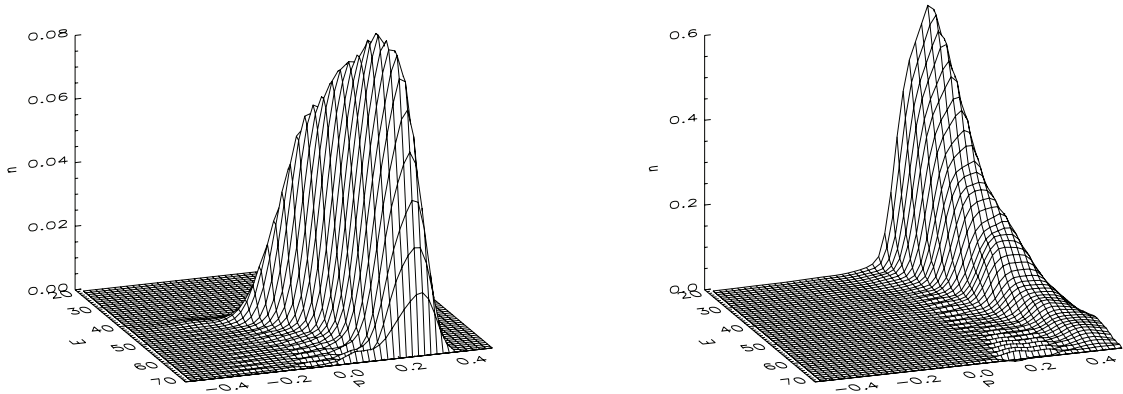

Figure 15. Examples of the two dimensional spline fits to f_0 for fixed μ. In the first plot $\mu B = 49$ keV, so particle energy is restricted to above this, and in the second $\mu B = 7$ keV. The energy ranges from 20 keV to 70 keV. Canonical toroidal momentum P_ζ, normalized to ψ_w, ranges from $-.5$ to $.5$.

mixing rate increases with island size and eventually equals the energy source rate, allowing a local flattening of the distribution within the island and eliminating the mode drive.

To carry out simulations of actual discharges, we need representations of the magnetic equilibrium, the high energy particle distribution, the spectrum of modes along with the eigenfunctions $\xi_{m,n}(\psi_p)$ and frequencies supplied by NOVA [9], values for collisional drag and scattering rates, and the drive terms resulting from partial derivatives of the particle distribution f_0. In NSTX typical beam injection is 6×10^{20} s^{-1}

and slowing down is from 20 to 100 ms, so the number in the beam is about 6×10^{19}. Transit time is typically three microseconds, so complete redeposition through beam injection occurs in 30 000 transits. Typical simulations are shorter than this, and also short compared to the pitch angle scattering time.

To advance the particle weights, we need the partial derivatives of f_0. The numerical method used is the following. Divide the space of $E, P_\zeta, \mu B$ into bins. With Monte-Carlo methods, develop a list of particles and construct a numerical
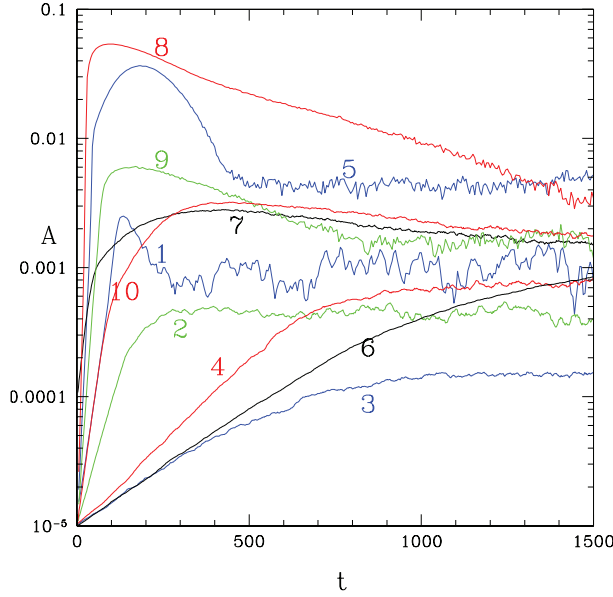
Figure 16. An example of time evolution of individual modes using NOVA damping rates with collision time of 200 ms. Shown is the amplitude versus time, with time in units of toroidal transits.
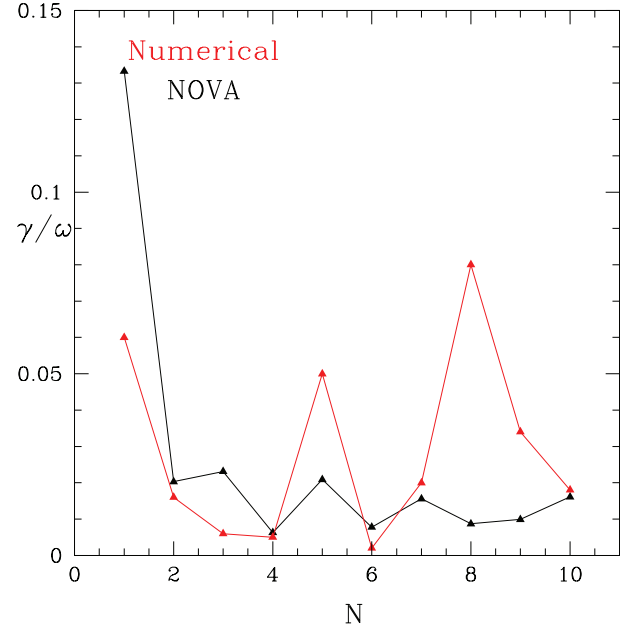

Figure 17. Numerical and NOVA growth rates.

Table 1. Modes observed in NSTX shot 141711 at $t = 470$ ms.

N	n	m	ω kHz	γ/ω	γ_N/ω	γ_d/ω	$10^3 A_{\mathrm{sat}}$	Harmonics
1	2	1–7	103	.138	.06	−.0047	1	1–7
2	3	2–10	104	.025	.016	−.0047	0.4	8–16
3	4	3–11	155	.027	.006	−.0039	0.15	17–25
4	4	3–11	158	.008	.005	−.001 68	0.8	26–34
5	4	2–10	125	.023	.05	−.0021	5	35–43
6	5	5–13	157	.008	.002	−.000 25	0.9	44–52
7	5	5–13	111	.017	.025	−.0014	1.5	53–61
8	5	3–11	116	.01	.08	−.0013	3	62–70
9	5	3–11	120	.013	.034	−.0031	1.9	71–79
10	6	7–15	116	.017	.018	−.0009	2	80–88

Note: Listed is the toroidal mode number n, the range of poloidal mode numbers, the frequency in kHz, the growth rates given by NOVA and by the present simulation, the damping due to the continuum and electron Landau damping, the saturated amplitudes, and the range of the harmonics included.

distribution $f_{E,P_\zeta,\mu}$. This can be done once at the beginning of the simulations, and it can be made smoother by advancing the initial distribution in time with a small collision frequency and slowing down operator, recording particle locations in bins every time step. However this distribution is not time independent. In any Hamiltonian system $H(p,q)$, the invariant phase space volume element is given by dpdq. In our case it is given for each value of μ by

$$\mathrm{d}P_\zeta \mathrm{d}P_\theta \mathrm{d}\theta \mathrm{d}\zeta \qquad (24)$$

so the time independent distribution function is the distribution in this space. Distributions are axisymmetric, so the variable ζ will be ignored. To find the correct time independent distribution function we must construct the Jacobian for the contraction from the space of dP_ζdP_θdθdμ to dEdP_ζdμ. Note that this is an irreversible contraction to a space of smaller dimension. The full particle distribution cannot be reconstructed given

$f(E, P_\zeta, \mu)$, which gives the space of all particle orbits but not the position of particles on the orbits. This Jacobian is found by loading particles uniformly in the space given by equation (24) and then finding their distribution in dEdP_ζdμ, which we donote by $J(E, P_\zeta, \mu)$. The correct time independent distribution function is then

$$f_0(E, P_\zeta, \mu) = f_{E,P_\zeta,\mu}(E, P_\zeta, \mu)/J(E, P_\zeta, \mu) \qquad (25)$$

This reduction is possible because only the changes in E and P_ζ are necessary to find the modification of the mode. Of course for evaluations of mode-particle energy transfer these quantities are evaluated at each particle location in the full four dimensional guiding center phase space ψ_p, θ, ζ, and $\rho_\parallel$, plus the value of μ.

An example is shown in figure 14 for the NSTX distribution for shot 141711 obtained from NUBEAM in TRANSP. An initial deposition of 300 000 particles was loaded and

advanced for 10^5 steps or 2000 toroidal transits, resulting in 3×10^{10} entries in the $50 \times 50 \times 50$ bins for $f_{E,P_\zeta,\mu}(E,P_\zeta,\mu)$. During the time evolution, very small values of collision and drag were employed in order to produce smoothing in the variables E and $/mu$. The particle energy ranges from 20 to 70 keV and μB from 0 to 70 keV. Note that the obtained distribution naturally attenuates above this energy, no significant population of high energy particles has been omitted. The canonical momentum P_ζ is normalized to ψ_w and ranges from -0.5 to 0.5. The Jacobian is then constructed by loading particles uniformly in $\theta, P_\theta, P_\zeta, \mu$ with Monte Carlo techniques and then binning them in E, P_ζ, μ to give $J(E,P_\zeta,\mu)$. This method produces a time independent initial distribution which, with additional smoothing, can be used to construct a spline fit.

The spline fit is made possible by observing that partial derivatives are needed only in the variables P_ζ and E, so for each value of μ a two dimensional spline is constructed. The spline representation requires nine coefficients at each of the 50×50 grid points, giving with 50 values of μ, a total of 1.125×10^6 coefficients to store for a given distribution. Examples of the obtained two dimensional splines are shown in figure 15. In the first plot $\mu B = 49$ keV and in the second $\mu B = 7$ keV. The energy range is from 20 keV to 70 keV, but since E must be greater than μB it is restricted to larger energies in the first plot. Canonical toroidal momentum P_ζ, normalized to ψ_w, ranges from -0.5 to 0.5. The marker particles were loaded uniformly in $P_\zeta, P_\theta, \theta, \mu$, giving a time independent distribution $g(E,P_\zeta,\mu)$ which is also uniform in E, P_ζ, μ, since this loading simply reproduces the Jacobian. Thus the stepping equation for the weight becomes

$$\frac{\mathrm{d}w}{\mathrm{d}t} = \frac{w-1}{g(E,P_\zeta,\mu)}[\partial_E f_0 \dot{E} + \partial_{P_\zeta} f_0 \dot{P}_\zeta]. \tag{26}$$

The use of a uniform distribution for g is much more accurate than having the marker distribution reproduce the actual particle distribution f_0 because there are large domains in the space of E, P_ζ, μ where f_0 is very small, and $\partial_E f_0/f_0$ can possess noise of order one.

The evolution of each mode was carried out separately, so there was no mode–mode interaction in these simulations. The simulations included pitch angle scattering and slowing down with time scales of 200 ms, probably somewhat higher than actual. Saturation amplitudes scale as $\nu^{2/3}$ so the obtained saturation levels are probably large, but in any case all modes must be advanced together in order to include mode–mode coupling and to compare with experimental values. The initial growth rate is given in the first 50 transits, and by 300 transits the growth rates for most modes have dropped to very small values. In this case the transit time is about three microseconds. The growth rate and the mode amplitude evolution are much smoother than in previous simulations [20, 22], in spite of the use in that case of analytic representations of the particle distributions, due to the noise free properties of equations (3) as well as the use of splined partial derivatives of the distribution.

Time evolution of individual modes is shown in figure 16, using 200 000 marker particles. All modes evolve to stable
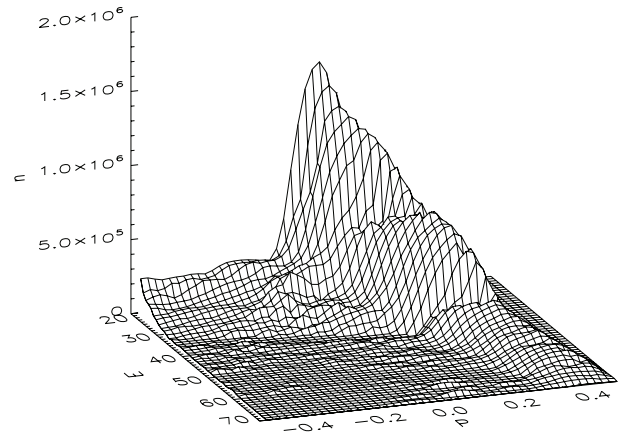

Figure 18. Distribution modification, for $\mu B = 21$ keV, mode 5, $n = 4$ and 125 kHz.

saturated levels. The final time for these simulations, equal to 5 ms, corresponds to a small fraction of a collision time, with $\nu T = .0025$

As seen in figures 2–11 a single mode produces resonance islands typically at several different locations in the plasma. Linear theory uses analytic resonance positions and it is not clear that all are completely or correctly given. But all resonance islands, unavoidable in a full simulation, and existing in the real plasma, can contribute either to the stabilization or destabilization of the mode, depending on the nature of the particle distribution.

In table 1 is shown the mode spectrum, giving the mode number N, the toroidal mode number n, the range of poloidal mode numbers, the mode frequency, and growth rate from linear theory as well as damping from the continuum and electron Landau damping. The entry γ_N is the numerically observed growth rate. All these simulations were carried out with collision and slowing down times of 200 ms, a collision rate somewhat larger than that in the NSTX discharge examined.

Figure 17 is a comparison of the growth rates given by NOVA and those obtained in the present simulation. The values of growth rate found by NOVA are often in disagreement with the values given in these simulations, with agreement for some modes only within a factor of five. The largest discrepancy in growth rate occurs for mode 8, which has principle resonances near the magnetic axis. Part of this disagreement can perhaps be ascribed to the fact that the distribution function used in NOVA was an analytic slowing down distribution. Thus it is perhaps the case that the present values are more reliable than those given by NOVA. But it is not clear that the present analysis of mode damping is sufficiently accurate to properly give the experimentally observed growth rates. As final results depend on collision rates, slowing down rates, and damping values, this must be regarded as a weakness of the present analysis as regards comparison with experiment. In addition, modes were advanced separately, there was no mode–mode coupling through modification of the particle distribution. Thus comparison of saturation amplitudes is not relevant at this point in the development of the model.
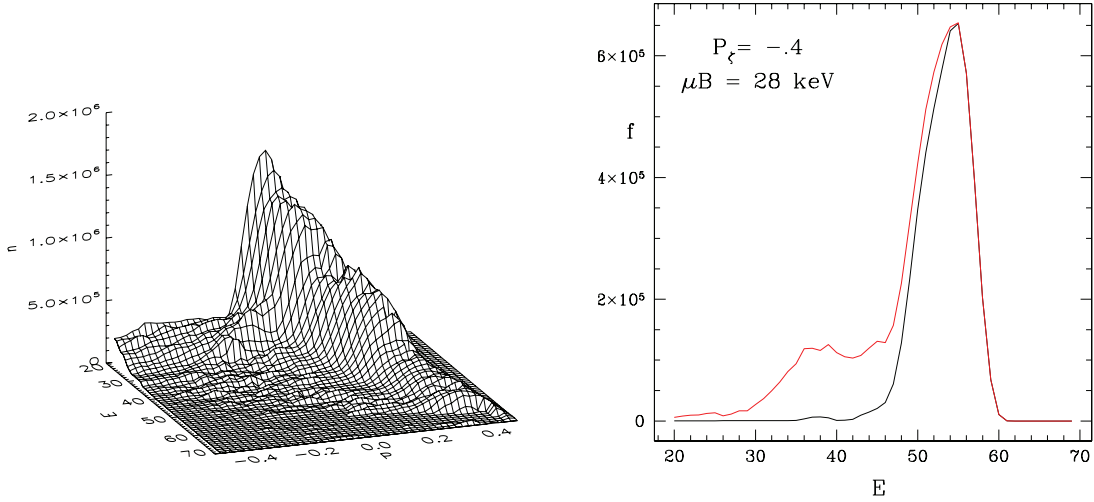
Figure 19. Distribution modification, for $\mu B = 28$ keV, and the change in the energy distribution for $P_\zeta/\psi_w = -0.4$, mode 8, $n = 5$ and 116 kHz.
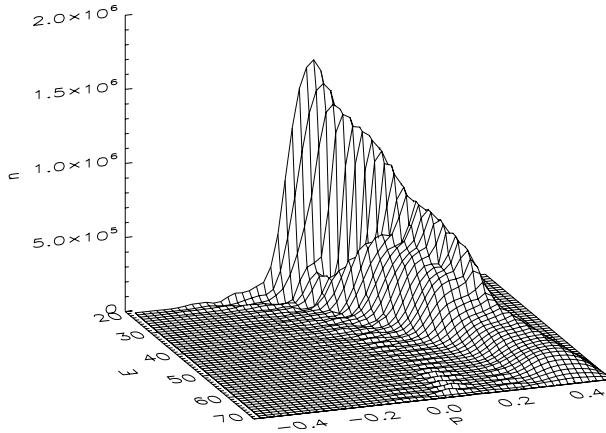

Figure 20. Distribution modification, for $\mu B = 21$ keV, mode 9, $n = 5$ and 120 kHz.
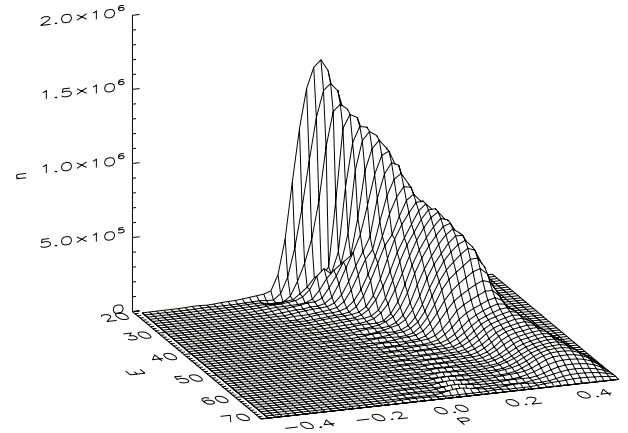

Figure 21. Distribution modification, for $\mu B = 21$ keV, mode 10, $n = 6$ and 116 kHz.

A simple model for mode saturation [23] gives

$$\omega_b = \frac{\nu_{\text{eff}}\gamma_L}{\gamma_d} \qquad (27)$$

with ω_b the bounce frequency in the resonance, γ_L the linear growth rate, γ_d the damping, and $\nu_{\text{eff}} = \nu(\omega/\omega_b)^2$ is the effective collision frequency. This expression is useful to compare scaling of saturation for a fixed mode with different values of collision frequency or damping. But in the present case each mode has its own unique resonance, and hence ω_b, and there is little information to extract using this expression. A separate publication [21] discusses saturation of a single mode as a function of collision frequency. See also [22].

8. Distribution modification

To find the distribution modification construct δf by sorting the test particles into bins in E, P_ζ, μ using weight w

$$\delta f(\psi_p, \theta, \zeta, \rho_\parallel, t)$$
$$= \sum_j w\delta(\psi_p - \psi_{p,j}(t))\delta(\theta - \theta_j(t))\delta(\zeta - \zeta_j(t))\delta(\rho_\parallel - \rho_{\parallel,j}(t)),$$

and obtain good statistics by averaging over a number of steps.

We then have

$$f(E, P_\zeta, \mu) = f_0(E, P_\zeta, \mu) + \delta f(E, P_\zeta, \mu)$$

where the two terms must be weighted acccording to the number of entries in each.

There is obviously an enormous amount of data available in the $50 \times 50 \times 50$ data points for the initial and the modified distribution functions, giving detailed information concerning the change of the distribution for each value of μ. Figures 2–11 give examples of the harmonics and the principle resonances, as well as example Poincaré plots. These, as well as the magnitude of the saturation amplitude, can be used to select domains of interest for distribution modification.

Examples of distribution modification are shown for modes 5, 8, 9 and 10 in figures 18–21. These show only the modification near $\mu B = 20$ keV, where the distribution is peaked. Similar plots can be obtained for all 50 values of μB. Other modes that saturate at small amplitude do not produce noticable modification of the beam distribution. In addition to these two dimensional plots, a distribution can be obtained in a single variable with the other two variables fixed. As an example in figure 19 is shown the initial and modified ditribution in energy, for fixed $P_\zeta/\psi_w = -.4$, $\mu B = 28$ keV.

A future publication will consider simulations with multiple modes present, interacting through the mutual modification of the distribution function. From the present results we conclude that modes saturating at low levels will probably not significantly affect other modes.

9. Conclusion

Alfvén modes driven unstable by energetic particles, either injected beam particles or fusion generated alpha particles, can evolve to amplitudes which produce large scale modification of the original high energy particle distribution. Thus it is critical to be able to estimate the saturation amplitudes of such modes in order to predict their effect on attempts to reach fusion producing temperature and density. This paper presents the initial development of a formalism and code capable of predicting saturation amplitudes using actual numerically generated equilibria, high energy particle distributions, and unstable mode eigenfunctions. A reduced noise means of evolving a spectrum of Alfvén modes up to saturation has been developed, using a spline representation of the observed particle beam distribution given by TRANSP and the spectrum of eigenmodes for this distribution given by NOVA. The beam distribution is fit with a spline function of E and P_ζ for each value of μ, allowing smooth partial derivatives in these first two variables. The low noise level of the simulations comes from the use of this representation of the beam distribution as well as the use of the exact mode-particle energy and momentum transfer given by equation (3). The method is illustrated using NSTX shot 141711. Poincaré plots and plots of phase vector rotation are used to understand and illustrate the resonance locations, and the δf method is used to examine the modified particle distribution. Several of the modes do not produce a significant modification of the initial beam particle distribution. These simulations represent only an initial exploration of the method. The modes were evolved one at a time, so mode–mode coupling through the particle distribution was not included. A future publication will explore multi-mode simulations, and also use improved values of collisions, drag, and damping, to better allow comparison with experiment.

References

[1] ITER Physics Basis Editors and ITER Central Team 1999 *Nucl. Fusion* **39** 2138
[2] Heidbrink W W 2008 *Phys. Plasmas* **15** 055501
[3] White R B, Gorelenkov N N, Heidbrink W W and Van Zeeland M A 2010 *Phys. Plasmas* **17** 056107
[4] White R B, Gorelenkov N N, Heidbrink W W and Van Zeeland M A 2010 *Plasma Phys. Control. Fusion* **52** 045012
[5] Van Zeeland M A *et al*, DIII-D and ASDEX Upgrade Teams 2011 *Phys. Plasmas* **18** 056114
[6] Collins C S, Heidbrink W W, Austin M E, Kramer G E, Pace D C, Petty C C, Stagner L, Van Zeeland M A, White R B and Zhu Y B 2016 *Phys. Rev. Lett.* **116** 095001
[7] Pankin A, McCune D, Andre R, Bateman G and Kritz A 2004 *Comput. Phys. Commun.* **159** 157
Pankin A, McCune D, Andre R, Bateman G and Kritz A 2009 *Phys. Plasmas* **16** 122505
[8] Gorelenkov N N, Cheng C Z and Fu G 1999 *Phys. Plasmas* **6** 2802
[9] Cheng C Z 1992 *Phys. Rep.* **211** 1–51
[10] Di Troia C 2012 *Plasma Phys. Control. Fusion* **54** 105017
[11] White R B 2014 *The Theory of Toroidally Confined Plasmas* 3rd edn (London: Imperial College Press)
[12] Kaye S M *et al* 2005 *Nucl. Fusion* **45** S168–80
[13] White R B, Spizzo G and Gobbin M 2013 *Phys. Plasmas* **20** 022105
[14] White R B 2011 *Commun. Nonlinear Sci. Numer. Simul.* 1906
[15] White R B 2011 *Plasma Phys. Control. Fusion* **53** 085018
[16] White R B 2015 *Plasma Phys. Control. Fusion* **57** 115008
[17] Kolmogorov A N 1957 *Proc. Int. Congress of Mathematicians (Amsterdam)* vol 1, p 315
Arnold V I 1963 *Russ. Math. Surv.* **18** 9
Moser J 1962 *Math. Phys. Kl.* II **Kl** 1
[18] Kaufman A N 1972 *Phys. Fluids* **15** 1063
[19] Mynick H E and Duvall R E 1989 *Phys. Fluids* **1** 750
[20] Chen Y, White R B, Fu G-Y and Nazikian R 1999 *Phys. Plasmas* **6** 226
[21] Zhou M and White R 2016 *Plasma Phys. Control. Fusion*
[22] Lang J, Fu G-Y and Chen Y 2010 *Phys. Plasmas* **17** 042309
[23] Berk H L, Breizman B N and Ye H 1992 *Phys. Rev. Lett.* **68** 3563